JOURNAL OF SPACECRAFT AND ROCKETS
Vol. 45, No. 6, November–December 2008

Active Vibroacoustic Device for Noise Reduction in Launch Vehicles

Steven Griffin[*]
Boeing–SVS, Inc., Albuquerque, New Mexico 87106
Steven A. Lane[†]
U.S. Air Force Research Laboratory, Kirtland Air Force Base, New Mexico 87117
and
Anthony Lazzaro[‡]
Boeing–SVS, Inc., Albuquerque, New Mexico 87106

DOI: 10.2514/1.36787

This paper presents the development of a noise mitigation device for launch vehicle fairings and the performance of the device as measured from sounding rocket experiments conducted by the U.S. Air Force Research Laboratory, Space Vehicles Directorate. A new modeling approach to predict the internal acoustic response particular to sounding rockets is presented wherein the interior noise results from the time varying accelerations acting through the forward bulkhead. This model is different from typical approaches used for payload fairing noise prediction in which the primary noise sources are the rocket motors. This model would also apply to rockets of a similar aspect ratio and acceleration profile. The active acoustic absorber presented in this work can be tuned for optimal performance just minutes before launch. Acceleration and acoustic measurements from two sounding rocket launches are presented to validate the modeling approach and to demonstrate the performance of the active acoustic absorber. Data showed that a single device achieved an 8.8 dB reduction in the sound pressure level from 20 to 300 Hz.

Nomenclature

Bl = loudspeaker force constant, N/A
c = loudspeaker viscous damping constant, $\mathrm{N \cdot s/m}$
$f(t)$ = loudspeaker applied force, N
K_f = filter gain
k = loudspeaker stiffness, N/m
L = loudspeaker inductance, H
m = loudspeaker mass, kg
P_{ref} = reference pressure, Pa
P_{rms} = pressure rms, Pa
R_{dc} = resistance, Ω
$v_a(t)$ = loudspeaker voltage, V
α = frequency shift ratio
ζ = loudspeaker damping ratio
ζ_f = low pass filter damping ratio
ζ_p = spring/mass/damper damping ratio
ζ_ϕ = bandpass filter damping ratio
ω_f = low pass filter resonance, rad/s
ω_p = spring/mass/damper resonance, rad/s
ω_ϕ = bandpass filter resonance, rad/s

I. Introduction

VIBRATION and noise loads during launch pose a significant risk to payload survivability. Government and industry have endeavored to understand and predict launch loads, develop coupled payload and vehicle models, and define adequate design standards and qualification tests to ensure that payloads survive launch. Currently, launch loads drive the structural and mechanical design of many payloads, which can result in overdesigned structures (i.e., excessively bulky) that thereby reduce the mass and volume available for scientific instruments, fuel cells, or maneuvering propellants [1,2].

Most of the mechanical vibration acting on the payload is generated by the rocket motor and transmitted through the adaptor ring. The vibration levels and spectra depend on the launch stack but are generally most severe over 20–2000 Hz, can be up to 7 g in the axial direction, and possibly have tonal components [3–5]. The vibration spectrum and amplitude varies during the vehicle's assent. Shock loads on the order of 1000 g can occur at separation events. The payload is usually “locked down” for launch in a stowed configuration to reduce its susceptibility to damage due to mechanical vibration.

The acoustic response within a payload fairing also varies depending on the launcher and fairing employed. The interior acoustics tend to be broadband (30–8000 Hz), between 130 and 145 dB (re: 20 μPa), and tonal due to acoustic resonances within the fairing [3–5]. Fairing acoustics tend to be worst during the first few seconds of launch (due to ground reflection of the thrust noise) and during transonic and maximum dynamic pressure events. Because the acoustic loads are so severe and coupling between the acoustic loads and the payload is uncertain, nearly all payloads must undergo some form of acoustic qualification testing. The modeling and simulation of the payload and launch loads are usually accomplished with statistical energy analysis models as a result of the high modal density of the acoustic volume and payload [6,7]. Typically, acoustic blankets are used to reduce fairing acoustic loads, but these are ineffective at some low-frequency limit. Below this limit, acoustic dampers have shown promise [8–10].

Acoustic dampers can be passive or active. Passive devices can incorporate passive diaphragm radiators or use damped Helmholtz resonators [11]. These devices are designed to couple with targeted acoustic resonances and, through this coupling, transform acoustic energy into heat. Active devices often use voice-coil-actuated diaphragms as used in loudspeakers. Active systems involve some form of closed-loop control to drive the dynamics of the actuator so that it presents dissipative impedance to the acoustic volume (as

---

Received 23 January 2008; revision received 26 June 2008; accepted for publication 5 July 2008.

[*] Boeing Technical Fellow, 4422 The 25 Way.

[†] Senior Aerospace Engineer, Space Vehicles Directorate, 3550 Aberdeen Avenue, Senior Member AIAA.

[‡] Electrical Engineer, 4422 The 25 Way.

opposed to reactive impedance). The performance of the acoustic damper depends on several factors, including the damping of the particular device, the damping of the target acoustic cavity resonance (s), the dimensions of the coupling surface relative to the acoustic volume, and the location of the device with respect to the acoustic mode shapes (i.e., spatial coupling) [12,13]. In the case of payload fairings, the device would need to be designed for a particular natural frequency and damping ratio, which must be based on unvalidated models, tested in a laboratory, and then finally qualified for launch. Optimization would be problematic, because it is difficult to accurately model fairing structural-acoustic dynamics and predict coupling between the device and payload volume. Additionally, conditions at launch, such as temperature and humidity, can affect target acoustic resonance frequencies and damping ratios, thus impacting performance. Therefore, a self-calibrating system that can adapt itself to the payload environment before launch provides a means to achieve optimal performance.

The motive for this work is to investigate a self-calibrating active acoustic control solution for reducing transmitted acoustics in launch vehicles that is effective at low frequencies, at which traditional passive treatments such as blankets show limited effectiveness and tuned active and passive absorbers are not sufficiently tolerant to changes in payloads and environmental conditions. An important constraint on the research was that the solution be amenable to a near-term hardware implementation. Further, the active acoustic device described in this work is the only one to the authors' knowledge that has been proven in a flight test.

II. Active Treatments

A. Control

It has been shown in laboratory experiments that a tuned, passive acoustic damper can provide several decibels of attenuation for a single acoustic resonance. However, the performance of diaphragm-type devices can be further enhanced by using feedback from a closely located microphone to command the volume-velocity response of the actuator [14]. A variation of this concept was presented by Olson and May as an acoustic sound absorber in 1953 [15]. Radcliffe et al. demonstrated a similar "acoustic sink" concept that used a loudspeaker to dissipate acoustic power in reverberant enclosures [16]. Work by Denoyer et al. demonstrated attenuation of the response of the fundamental acoustic resonance by 26 dB in a subscale composite fairing test article using a single acoustic actuator located at the nose of the structure [17]. Denoyer et al. used a second-order, positive-position feedback controller and a microphone as the control sensor. Later work by Lane et al. used spatially weighted arrays of sensors and volume-velocity actuators to actively damp the first five acoustic resonances in an aircraft fuselage [18]. Lane et al. used an H_2 dynamic feedback controller based on a time-domain system identification of the structural-acoustic system. Their approach was later successfully demonstrated on a fiberglass payload fairing test article [19].

Realizing the importance of superior performance that is tolerant to changes in system behavior, the approach demonstrated in this paper uses a simplified, single-input/single-output controller with a low-order discrete feedback control filter based on a previous work by Denoyer et al. [17]. The control system was designed to autonomously measure the frequencies of selected acoustic resonances while on the launch pad and, from that, compute and implement a feedback controller. The control system could self-tune minutes before launch, providing improved performance over a static controller designed in a laboratory. The simplicity of the controller reduced implementation risk and resulted in a solution that was more tolerant to change than more elaborate control schemes.

B. Sounding Rocket

A flight-qualified system was developed and flown on a sounding rocket experiment. A sounding rocket is a small, relatively low-cost, suborbital test vehicle typically used for scientific/atmospheric research or as a target vehicle by the military. Two sounding rocket launches formed the Vibro-Acoustic Launch Protection Experiment (VALPE) program [20,21]. The goal of the VALPE program was to develop prototype hardware and demonstrate four previously unflown technologies for mitigating launch loads: 1) a chamber-core composite fairing, 2) a hybrid passive/active isolation system, 3) a regenerative isolation system, and 4) a low-frequency acoustic damper. The first flight, VALPE-1, was instrumented to collect baseline data on the flight environment using a variety of microphones, dynamic pressure sensors, accelerometers, and strain gages. VALPE-2 had a virtually identical sensor package and carried the four experiments. To maintain similarity between VALPE-1 and VALPE-2, VALPE-1 included "simulated" payloads of similar mass and volume as those flown on VALPE-2. Figure 1 shows a schematic of the VALPE-1 sounding rocket and payload fairing. The crosshatched portions in Fig. 1 indicate the locations of the mass simulators. A photograph of the VALPE-2 vehicle on the launch rail at the Wallops Island launch site is given in Fig. 2. Both vehicles were successfully launched and now currently reside in the Atlantic Ocean somewhere off the coast of Virginia.

C. Overview

This paper will first present a model to predict the internal acoustic response of a sounding rocket in which the interior acoustic response is driven by the axial, time varying accelerations. This response is significantly amplified by the axial resonant behavior of the mass loaded nose cone with the fairing acting as an axial spring. Next, the design and development of the active acoustic absorber system, feedback controller design, and simulations on a fully coupled structural-acoustic model are presented. This paper presents the first known use of the modal interaction method to predict the passive and active effects of a specific acoustic control device in a sounding rocket and the first known acoustic transmission model to accurately predict the acoustic response in a sounding rocket fairing. Results from VALPE-1 and VALPE-2 are presented to validate the modeling approach and demonstrate the performance of the active acoustic damping system.

III. Theory

First, it was necessary to develop a specialized vibroacoustic model of the sounding rocket payload volume coupled with the active acoustic absorber. The following analysis tasks will be addressed in this section: 1) the modeling of sounding rocket noise transmission, 2) the coupling of a voice-coil actuator to the fairing model, 3) the development of active damping controllers, and 4) coupled simulations and analysis.

Task 1 required new theoretical development not found in the literature, but was subsequently verified by launch data. Tasks 2–4

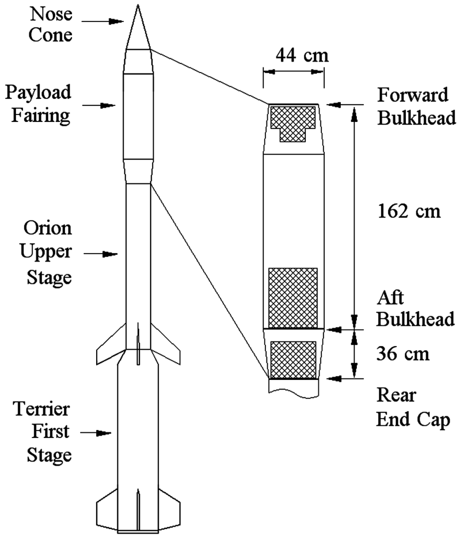

Fig. 1 Schematic of the VALPE-1 sounding rocket and payload fairing.

Fig. 2 VALPE-2, preparing to be launched.

leveraged existing technology that was applied to the sounding rocket experiment.

A. Sounding Rocket Transmission Model

A payload fairing is essentially a flexible structure enclosing an air volume. Typically, the interior acoustics of such a system can be modeled using the modal-interaction approach with in vacuo structural modes and rigid wall acoustic modes. Specifically, the out-of-plane motion of the fairing walls resulting from bending and ring modes couple into the air volume. External excitation of the fairing results from external acoustics that occur during the launch and from the direct excitation of the fairing via vibratory flanking paths. A mathematical representation of this behavior can be used to evaluate low-frequency structural-acoustic transmission for a given applied external load [22]. However, for a sounding rocket, this paradigm is not supported by measured data. Because the smaller launch vehicle takes off so swiftly from the launch pad, there is only a very brief period (less than 1 s) during which the external noise from the motor can excite the fairing acoustics (the launch of a sounding rocket has been qualitatively described as being like the launch of a “bottle rocket”). Rather, it is hypothesized that transients from the axial acceleration of the launch vehicle drive (vibrate) the nose-cone bulkhead assembly, which, in turn, drives the acoustic response within the payload volume.

To predict acoustic transmission, a finite element model of a laboratory mock-up was modeled with approximately the same width and length of the actual sounding rocket. The mock-up was used because extensive testing of the device control algorithm was accomplished in the laboratory before the flight. The mock-up was close enough to the flight hardware to give a reasonable representation and allowed extensive instrumentation for comparisons between the modeled and measured quantities. The transmission model included representations of the acoustic space and of the nose-cone bulkhead assembly. The mock-up was a heavy cardboard cylinder. A three-dimensional drawing with volume reserved for the device, along with a drawing of the cylinder, was used to generate a finite element model of the acoustic space. The NASTRAN acoustic finite element model had 49,841 tetrahedron elements and 79,093 nodes. A cross section of the finite element model is shown along with the pressure distribution of the first uncoupled acoustic mode in Fig. 3. The measured, uncoupled axial frequency of the hardware mock-up of 114 Hz was very close to the predicted frequency of the model of 114.5 Hz. Figure 3 shows a high acoustic pressure associated with the first mode in the region of the device diaphragm. This is a good indication that there will be strong coupling between the active/passive acoustic absorber and the first acoustic mode.

The modal interaction method as modified for use with the NASTRAN results provided the means to couple the rigid wall acoustic modes to the in vacuo structural modes of interest [23]. For the transmission model, the structural mode was limited to the axial resonance of the nose-cone assembly at 138 Hz. The measured weight of the nose-cone assembly of 38.3 N was smeared into rigidized plate elements, and the stiffness of the fairing was represented by a spring element, the value of which was derived from the measured nose-cone assembly resonance of 138 Hz. The modal damping in the system was defined to be 1% for the acoustic and nose-cone assembly modes, 4% for the diaphragm mode, and 5% for the nose-cone assembly based on measured data.

To investigate the role of the oscillation of the nose-cone assembly in generating acoustics on the interior of the sounding rocket, an enforced acceleration problem was formulated. The fairing model was constrained at the base, where it attached to the relatively rigid rocket motor. The measured acceleration during the first 0.3 s of launch was used to provide an enforced input at the base. The transient pressure predicted at the nose microphone was then converted to a power spectrum for comparison with the actual measure data from flight 1. This comparison is shown in Fig. 4.

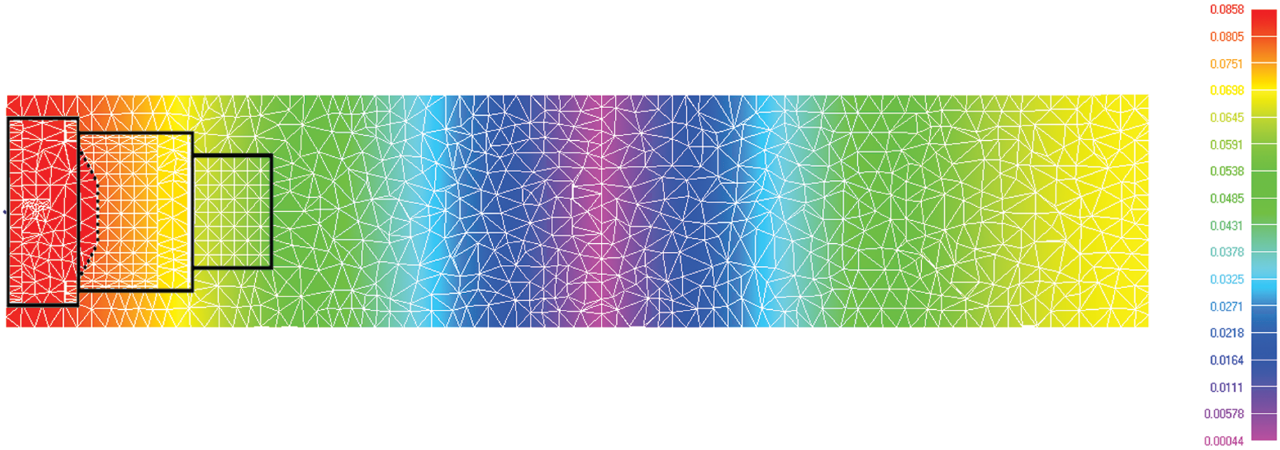

Fig. 3 Finite element model of the cylinder with the first uncoupled acoustic mode illustrated.

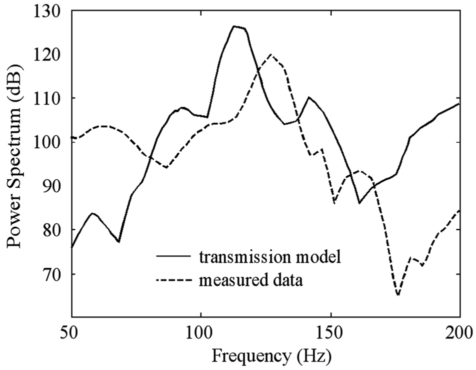

Fig. 4 Measured vs predicted levels.

Considering the differences in the model and the actual flight, the two curves in Fig. 4 show remarkable similarity. Both exhibit a clearly defined maximum that is coincident with the first axial acoustic mode of 114 Hz in the case of the transmission model and 127 Hz in the case of the measured data from the rocket. Also, the overall rms values of 130 dB for the transmission model and 124 dB for the fight experiment were relatively close. In both the predicted and measured results, over 98% of the overall rms magnitude was accounted for in the frequency range of 50–200 Hz. The disagreement in amplitude was most likely the result of an underprediction in the damping ratio of the first acoustic mode, which appeared to be higher in the flight data. Considering the agreement in magnitude and character of the model prediction and the flight data, the primary mechanism for sound transmission into the payload was likely the axial motion of the nose-cone assembly. This is dramatically different from the explanation of sound transmission in orbital launch vehicles, wherein the primary low-frequency mechanism is acoustic excitation and the subsequent motion and radiation of sound by the launch vehicle fairing. It also illustrates the point that a great deal of noise reduction can be achieved by adding damping to the first axial acoustic mode in a sounding rocket.

B. Active Acoustic Absorber Modeling

Although the exact payload configuration and resonance frequencies of the VALPE-2 system were unknown before launch, measurements from VALPE-1 were used to design an active acoustic absorber system to target the first and second acoustic resonances. The primary component of the acoustic absorber was a voice-coil audio speaker. The first step of the design process was to set the fundamental resonance (piston-mode) frequency of the speaker (and mounting enclosure) proximal to the expected first acoustic resonance of the fairing (i.e., about 130 Hz). This was accomplished by designing the mounting enclosure to provide sufficient air-spring stiffness, which was a function of the enclosure volume, the loudspeaker diaphragm cross-sectional area, and the inherent compliance of the loudspeaker.

The loudspeaker and enclosure can be modeled as a second-order system at a low frequency. Given a loudspeaker with diaphragm mass m, viscous damping c, and effective suspension and enclosure stiffness k, the diaphragm displacement, $x(t)$, can be given as a function of applied force, $f(t)$:

$$m\ddot{x}(t) + c\dot{x}(t) + kx(t) = f(t) \tag{1}$$

Electrodynamics can be added to the model by relating the applied force to the current in the voice coil:

$$f(t) = Bli(t) \tag{2}$$

The voice-coil current is a function of the voltage applied to the voice-coil terminals, $v_a(t)$; the coil inductance, L; the static coil resistance, R_{dc}; and the force constant, Bl. This results in the following coupled differential equations:

$$m\ddot{x}(t) + c\dot{x}(t) + kx(t) = Bli(t) \tag{3}$$

$$v_a(t) = L\frac{\mathrm{d}i(t)}{\mathrm{d}t} + R_{dc}i(t) + Bl\dot{x}(t) \tag{4}$$

Models were developed using the parameters of a commercially available, 20.3-cm-diam (8 in.) high-performance loudspeaker with a high-density neodymium magnet, which was selected as the acoustic actuator for the flight experiment.[§] The force constant, Bl, was experimentally measured, and other parameters were inferred by curve-fitting measured data. In practice, a power amplifier is used to command a voltage across the voice-coil terminals. The power amplifier essentially closes the circuit between the voice-coil terminals. The amplifier appears as a low-impedance load to the voice coil, and so diaphragm motion can induce current flow. As a result of the electromechanical coupling, the passive damping of the speaker increased from $\zeta = 0.035$ (open circuit) to 0.33 with an amplifier attached.

C. Coupled Structural-Acoustic Model Development

The next step was to couple the actuator model with the structural-acoustic model. This was accomplished by adding an additional radiating surface to the structural-acoustic model to represent the speaker diaphragm and an additional vibration mode to the structural model. The dynamics of the actuator model come from Eqs. (3) and (4).

To validate the model, the transfer function between a voltage into the speaker and the pressure measured at the location of the control microphone in the model is shown in Fig. 5 with both magnitude curves normalized. This is necessary for comparison because the control microphone was not calibrated. Considering no tuning of the model was performed to match the measured data, this agreement was quite good and more than adequate for initial control development using the analytically derived model.

D. Feedback Control Approach

By sensing the actuator output (acoustic pressure, voice-coil current, or even diaphragm motion) and implementing a feedback loop to the applied voltage, the effective stiffness and damping of the actuator can be adjusted to improve coupling and energy dissipation at the target enclosure resonance. Using a dynamic compensator (with poles and zeros, not just a static gain), the actuator can be used to target and attenuate multiple acoustic resonances.

A proven approach to provide damping on structures is positive-position feedback (PPF) control. This control approach is particularly applicable if the target resonances are separated in frequency (not strongly coupled), as are the low-frequency acoustic modes of the payload fairing. Fanson and Caughey present a good description of positive-position feedback with a stability analysis [24]. Friswell and Inman generalized the positive-position feedback control approach for multi-input/multi-output systems and related PPF filter design to the design of an optimal output feedback controller [25]. Bronowicki et al. presented the application of PPF controllers using piezoceramic actuators on a large test structure for vibration control [26]. Denoyer et al. presented the development and use of PPF controllers as part of a structural-acoustic control approach for controlling noise transmission using a subscale payload fairing [17]. The controller used in the sounding rocket experiment was based on that work, and so the theory and design approach will be briefly presented here.

A PPF controller is essentially a single-input/single-output second-order control filter that can be expressed as follows:

$$H(s) = \frac{K_f\omega_f^2}{s^2 + 2\zeta_f\omega_f s + \omega_f^2} \tag{5}$$

[§] Lanzos NEO-8, $f_s = 37$ Hz; $V_{\mathrm{as}} = 0.025\ \mathrm{m}^3$; $Q = 4.7$; $m = 37$ g; $Bl = 7.75$ N/A; $R_{\mathrm{nominal}} = 4\ \Omega$; $L = 0.73$ mH.

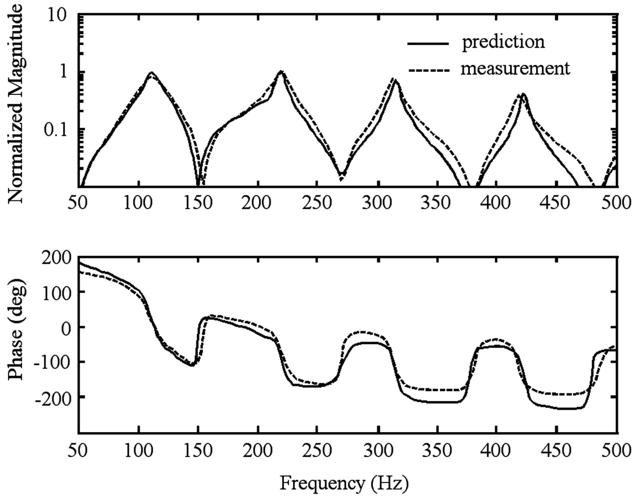

Fig. 5 Comparison of predicted and measured data.

where K_f is the filter gain, ω_f is the control filter resonance frequency (rad/s), and ζ_f is the control filter damping ratio. The tuning rules usually followed to determine the control filter resonance, damping ratio, and gain start with setting the control filter frequency, ω_f, equal to the target acoustic resonance frequency, ω_p. Next, the damping of the filter, ζ_f, is set to approximately twice that of the *desired* closed-loop damping (understanding that effectiveness is dependent upon coupling, which is strongly affected by the damping ratio). Finally, the gain, K_f, is increased to minimize the response at resonance (i.e., the closed-loop poles are set to minimize the amplitude response over an arbitrary bandwidth about the target resonance frequency). The objective of the PPF controller is to draw the lightly damped poles of the system away from the imaginary axis, thus adding damping to the poles in the closed-loop system. As the name implies, the input to the controller is displacement. The controller gain is largest at filter resonance, with the amplitude rolling off at frequencies higher than ω_f. For a second-order spring-mass-damper system such as

$$G(s) = \frac{\omega_p^2}{s^2 + 2\zeta_p\omega_p s + \omega_p^2} \tag{6}$$

where ω_p is the natural frequency and ζ_p is the damping ratio, the displacement coordinate is -90 deg relative to the input at resonance. Then, $H(s)$ contributes another -90 deg at resonance, which effectively yields a loop gain of $G(s)H(s) = -180$ deg at resonance. Closed-loop performance (damping) will be reduced if this relation is not maintained. This control approach only requires a priori knowledge of the resonance frequency to be controlled and its damping ratio, eliminating the need to perform wideband system identification (a significant reduction in computation, complexity, and risk).

For the coupled sounding rocket system, this approach is somewhat problematic because of the additional phase delay introduced by the actuator electrodynamics, the imperfect collocation of the sensor and actuator, and the phase delays resulting from the discrete controller implementation (i.e., sample and hold, computation delay). To use this control approach with a plant for which the phase at resonance is not an integer multiple of 90 deg, the controller must provide a phase contribution to compensate for the deviation in phase from 90 deg as well as the 90 or 270 deg shift from the PPF filter (depending on the sign of the resonance). This compensation amounts to a tailored time delay or advance that is fed back through to implement rate damping at the frequency of a selected resonance. Implementation of the additional time delay can be accomplished many different ways, from a straightforward delay at the frequency of interest in a digital filter implementation to a Padé approximation of a delay in a continuous implementation. Both of these approaches would require a bandpass filter to limit spillover and selectively control gain at the frequency of interest. A practical way of implementing such a compensator that is directly traceable to an analog implementation is with a damped bandpass filter, which yields $H'(s)$:

$$H'(s) = \left(\frac{K_f\omega_f^2}{s^2 + 2\zeta_f\omega_f s + \omega_f^2}\right)\left(\frac{2\zeta_\phi\omega_\phi s}{s^2 + 2\zeta_\phi\omega_\phi s + \omega_\phi^2}\right) \tag{7}$$

where ω_ϕ and ζ_ϕ are the natural frequency and damping ratio of the bandpass filter, respectively. The bandpass filter frequency can be tuned to add or subtract phase from the control filter. The additional phase added by $H'(s)$ can be expressed as a function of the shift ratio, denoted here as $\alpha = \omega_\phi/\omega_f$. The phase difference is given as

$$\Delta\phi = \angle\frac{H'(s)}{H(s)} = \angle\frac{s2\zeta_\phi\omega_\phi}{s^2 + 2\zeta_\phi\omega_\phi s + \omega_\phi^2} \tag{8}$$

Substituting $s = j\omega$ and $\omega_\phi = \alpha\omega_f$ yields

$$\Delta\phi = \angle\frac{2\zeta_\phi\alpha\omega_f j\omega}{(j\omega)^2 + 2\zeta_\phi(\alpha\omega_f)(j\omega) + (\alpha\omega_f)^2} \tag{9}$$

At resonance, $\omega = \omega_f$, which yields

$$\begin{aligned}\Delta\phi &= \angle\frac{j2\zeta_\phi\alpha}{(\alpha^2 - 1) + j2\zeta_\phi\alpha}\\ &= \angle\frac{-2\zeta_\phi\alpha}{-2\zeta_\phi\alpha + j(1 - \alpha^2)} = \tan^{-1}\left(\frac{\alpha^2 - 1}{2\zeta_\phi\alpha}\right)\end{aligned} \tag{10}$$

For a required $\Delta\phi$, Eq. (10) can be solved for the corresponding shift ratio, α, using a root-finding method (such as Newton's method). Figure 6 shows the phase difference (at resonance) as a function of the shift ratio, assuming $\zeta_\phi = 0.5$.

Considering the first mode of the transmission model, the phase at the 110 Hz fundamental mode is 28 deg due to the coupling with the actuator. This represents a delay of 62 deg beyond the expected 90 deg at resonance. Solving Eq. (10) for a positive phase of 62 deg gives a shift ratio of 2.2. The resulting filter is placed in series with the control filter designed using the standard PPF rules. A unity-gain bandpass filter with the same damping and frequency as the PPF filter can also be added in series to limit spillover. This addition does not change the phase or magnitude introduced by the control filter at the first mode frequency, but it does increase the order of the filter to the sixth order. Figure 7 shows the closed-loop behavior designed using the modified method that compensates for the delay and the tuning rules without compensation. Because this approach applies the PPF approach to a much broader set of plants, the compensated result is referred to as generalized active damping (GAD). Although the GAD approach adds damping to the peak, because of the added phase delay the traditional PPF approach actually takes away damping and destabilizes the resonance.

This example can be used to generate a slightly modified set of tuning rules that are amenable to an automated implementation for actively damping a system with phase delay at resonance. To implement GAD, find the value of the phase at the target resonance, ω_p, and compute the additional phase needed. This determines the shift ratio, ω_ϕ/ω_f, thus defining ω_ϕ. ζ_ϕ can be defined as some convenient value such as 0.5. Then, set $\omega_f = \omega_p$ and ζ_f to some practical value greater than ζ_p. Finally, adjust the gain to minimize the response about ω_p and implement the bandpass filter, if necessary, to minimize spillover. This approach can be applied sequentially to all peaks of interest in a given frequency band in an automated fashion. Figure 8 gives the resulting closed-loop plant with GAD applied sequentially to all peaks in the band from 0 to 500 Hz. In this case, all the peaks benefit from additional damping in the closed-loop result.

E. Coupled Model Simulations

Closed-loop simulations will now be presented that apply the control approach developed in the previous section to the coupled structural-acoustic-actuator model. A block diagram of the closed-

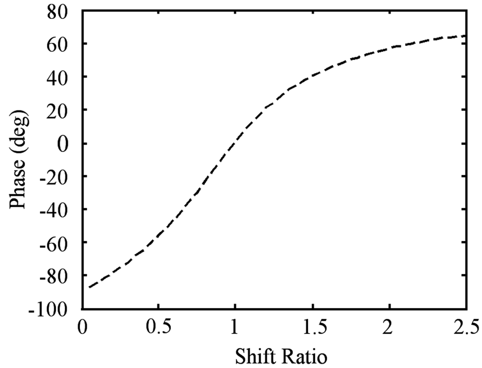

Fig. 6 Phase added (or subtracted) by the bandpass filter in the augmented controller, $H'(s)$, as a function of the shift ratio, ω_ϕ/ω_f.

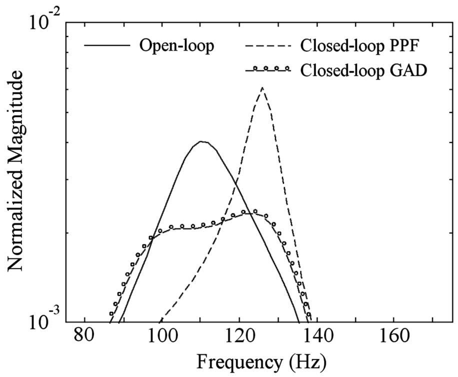

Fig. 7 Closed-loop result with and without compensation for phase delay.

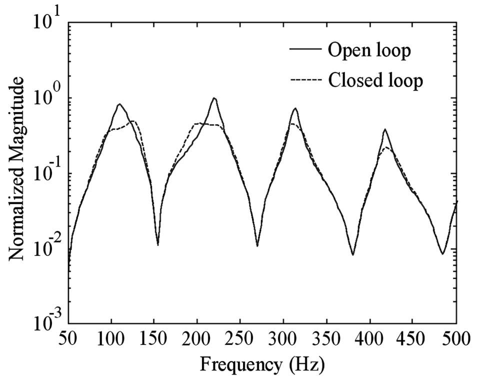

Fig. 8 Closed-loop plant with GAD applied sequentially to all peaks in the band from 50 to 500 Hz.

loop system architecture is shown in Fig. 9. $\{A, B, C, D\}$ represent the state-space realization of the open-loop system. Output $y(t)$ represents the acoustic response at a point close to the actuator that was used for feedback. The performance metric, denoted as $z(t)$, represents the spatially averaged acoustic response from 320 points distributed throughout the acoustic volume. The control law $H'(s)$ targets only the first acoustic mode.

Finally, the structural-acoustic model may be used to investigate whether adding the vibroacoustic device to the launch vehicle will reduce the interior acoustics when subjected to the predicted launch acoustic loads. Figure 10 shows a comparison of predicted power spectra at the nose microphone during the first 0.3 s of the launch with and without the vibroacoustic device. The figure also shows the effect of the vibroacoustic device with and without the active control loop on. Adding the device to the acoustic space results in a predicted 5.5 dB rms reduction in the band from 50 to 500 Hz. Closing the control loop results in a modest additional 1.2 dB rms reduction over the same range, resulting in a total predicted reduction of 6.7 dB rms for the active device.

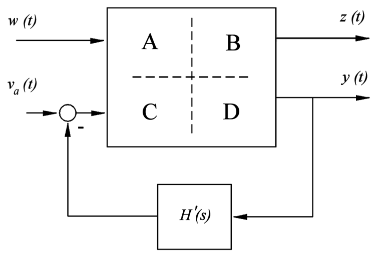

Fig. 9 Block diagram of the closed-loop system architecture.

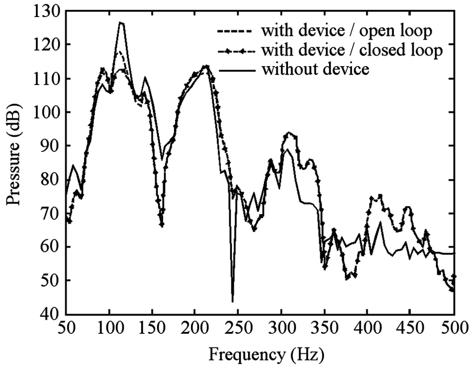

Fig. 10 Predicted power spectrums due to launch loads with and without the active and passive device.

IV. Prototype Controller Development

In VALPE-2, the acoustic absorber and control system were mounted in the forward end of the payload fairing, with the diaphragm pointed forward to maximize coupling with the acoustic modes. There was a separation of approximately 10 cm between the rim of the diaphragm and the forward end cap, shown in Fig. 11, provided by six "stand offs" that were circumferentially located. The resulting loudspeaker and enclosure system had a fundamental resonance frequency of about 130 Hz.

Also shown in Fig. 11 is a control microphone above the speaker diaphragm that was used as an error sensor for the control system (i.e., $y(t)$ in Fig. 9). The hardware for the control system and power supply (battery) was attached to the bottom of the speaker enclosure via four vibration isolators. The controller included a microprocessor, signal conditioning hardware, analog-to-digital converters, RAM, EEPROM, and a digital-to-analog converter. A real-time Linux operating system installed on a Pentium-based PC104 motherboard was selected for the flight controller. MATLAB® Simulink and Real-Time Workshop were used to develop simulations and generate flight software for the experiment [27,28].

The prototype system was tested on a laboratory mock-up of the fairing to verify algorithms, test the software, and determine initial values for the compensator gain, K_f, and other design parameters. On

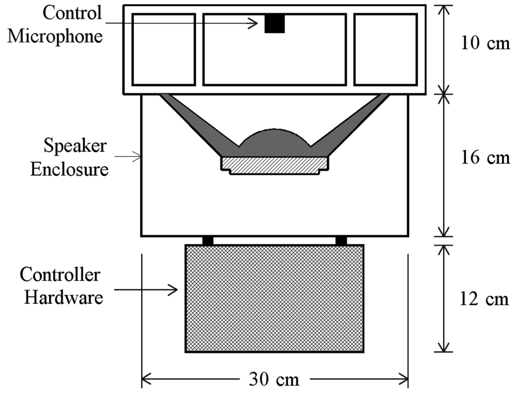

Fig. 11 Schematic of the diaphragm absorber and enclosure.

boot up, the controller performed an initial training task in which a band-limited burst-chirp sequence was applied to the actuator and the resulting control microphone signal measured. The onboard processor then performed a fast Fourier transform on the signals, and the resonance frequencies and damping ratios of the first two acoustic modes were identified. From these measurements, the parameters for the controller were set (including ω_f, ζ_f, ω_ϕ, and ζ_ϕ). The controllers were implemented using the sequential loop closure method demonstrated in the previous section. The control filter gains were adjusted to minimize the closed-loop rms response over the 300 Hz bandwidth. This automatic training process was initiated by a signal from the ground station in the minutes just before launch. The complete device (including the controller hardware) had to meet a total mass requirement of 13.6 kg ± 1% to enable a stable ballistic trajectory of the rocket.

V. Flight Experiment

All flight hardware was required to pass vibration environment *acceptance* testing, and all hardware not previously flown on a sounding rocket (mass simulators, experiments, and sensors) was required to pass additional vibration *qualification* testing before being used on a sounding rocket, per NASA regulations. The Terrier–Orion acceptance test levels were 13.6 g rms for band-limited random (20–2000 Hz) testing. Qualification test levels were 20.4 g rms for band-limited random testing. These test requirements drove most of the experiment's structural considerations and transducer selection. The articles used for the qualification testing were not flown, but were kept as backups. The actual flight hardware was only subjected to acceptance loads. Figure 12 shows the VALPE-2 payload fairing on the shaker table before qualification testing. The qualification test loads and acceptance test loads were more severe than the actual measured flight loads (i.e., longer in duration). Many components did not survive testing, and significant time and effort was expended troubleshooting and repairing the various experiments after vibration testing. Data measured from the VALPE-1 base-vibration qualification testing revealed a high-amplitude axial structural resonance near 138 Hz that resulted from the mass of the nose cone supported by the stiffness of the fairing assembly (stretching and compressing the fairing in the axial direction). This observation was important to interpreting and understanding the VALPE-1 flight data and modeling the acoustic response.

A total of 13.6 kg was allocated for all hardware related to the acoustic damper experiment. Although the total components weighed much less than 13.6 kg, the remaining allocation was used to reinforce the structure to survive qualification testing. Some components, such as the actuator and microphones, were designed to withstand the vibration testing directly, whereas the more sensitive equipment, such as the control computer and signal conditioners, were placed on isolation mounts to reduce the intensity of the vibration to which they would be exposed.

A fixed number of telemetry data channels were available on each flight. Used in each flight were 12 acoustic transducers, which were mounted in the front, mid, and aft sections of the fairing.[¶] Microphone positions within the fairing were kept as consistent as possible between the two flights to allow for comparison of the data. Sensor measurements were input into a charge amplifier and signal conditioning system and then downlinked to the ground station. Not all measured data were usable due to dropouts and sensor, conditioner, and telemetry malfunctions. Acoustic data was sampled at 5 kHz using 16 bit discretization. Most accelerometers were sampled at 5 kHz, with a few sampled at 10 kHz.[**] For analysis, measurements were converted from integer values (ranging from 0 to 216) to signal voltage (0 to 5 V). The measurements were then converted to physical units using calibration information measured in the laboratory before payload integration.

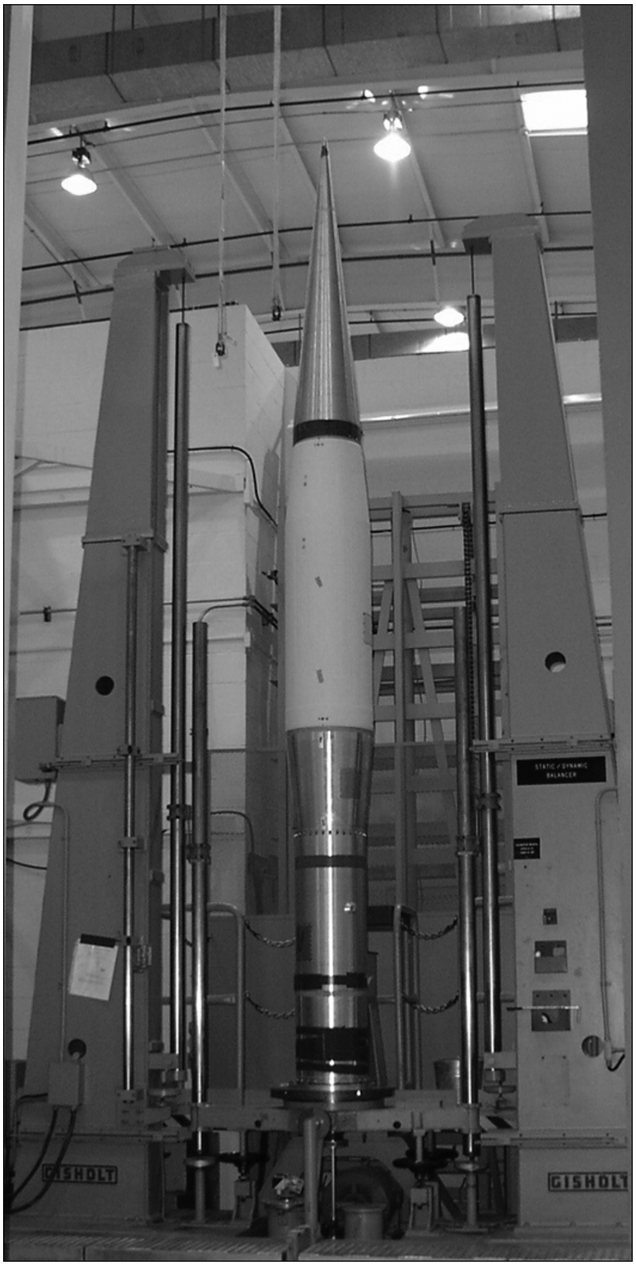

Fig. 12 VALPE-2 aft assembly, payload fairing, and nose-cone assembly in the vibration test stand.

Acoustic measurements were high-pass filtered (in MATLAB®) using a fourth-order Butterworth filter (with a cutoff frequency of 20 Hz) to remove some of the very-low-frequency energy and dc bias in the signals. With the dc bias removed, the signals were ±2.5 V. Signal clipping and data dropouts did occur, appearing as high-frequency events, and were not eliminated by the filtering process. Thus, some postfiltered data points did exceed the ±2.5 V range, which introduced some, albeit small, error. Time-domain measurements from both flights were analyzed in the frequency domain using MATLAB®.

A. VALPE-1 Experiment Results

A synopsis of the flight events is given in Table 1. The entire flight lasted only about 7 min. The vehicle became supersonic within the first 3 s of flight. Data for the first 100 s is presented in Fig. 13 for a single (forward) microphone. The second-stage ignition at $T = 20$ s is very noticeable in the time history. The rms response of each

---

[¶] GRAS Model 40BD; sensitivity = 1.6 mV/Pa@250 Hz, frequency range = 10–70 kHz, and dynamic range = 45–174 dB.

[**] PCB shear accelerometer model 357A05; sensitivity = 17 pC/g, maximum frequency = 10 kHz, dynamic range = ±500 g (peak to peak), and capacitance = 1600 pF.

Table 1 Timeline of expected flight events for the VALPE launches

Event	Time, s	Altitude, km	Velocity, m/s
Rail exit	0.4	0.0	46.5
First-stage burnout	5.2	2.0	714.6
Second-stage ignition	20.0	9.6	386.1
Second-stage burnout	45.4	36.3	1388.3
Second-stage separation	85.0	81.7	1022.8
Flight apogee	187.0	138.0	348.5
Ballistic impact	408.0	0.0	135.8

microphone was computed over 0.1 s intervals. Then, for each 0.1 s interval, the mean rms response over all microphones was computed. From this "spatial average," the sound pressure level was computed relative to $P_{\text{ref}} = 20\ \mu\text{Pa}$:

$$\text{SPL} = 20 \times \log_{10}\left(\frac{P_{\text{rms}}}{P_{\text{ref}}}\right) \tag{11}$$

and given in Fig. 14. This provides a rough estimate of the mean interior response as a function of time. The interior level peaked at about 113 dB during the first second of launch. There was an event at about 6 s that was measured by all microphones. Although the cause of this event is uncertain, the time history given in Fig. 13 indicates a peaking of the response at about this time.

Figure 15 presents the low-frequency (0–500 Hz) power spectral density for the spatially averaged microphone response for the first second after ignition. The data show the fundamental acoustic mode at approximately 127.3 Hz, with the response quickly rolling off above this frequency. The second acoustic resonance appears to occur at about 246 Hz and the third at approximately 389 Hz. Notice the significant amplitude difference between the power spectral density at the fundamental acoustic mode and the higher-order acoustic modes (almost 3 orders of magnitude).

Figure 16 presents the spatially averaged sound pressure level (computed over one-third-octave bands) for the first second of launch and for the interval from 20 to 21 s. The overall sound pressure level was 107.2 dB from 0 to 1 s and 101.4 dB from 20 to 21 s. Levels are higher than those shown in Fig. 14 due to the longer time interval used in these computations. Comparing the two, the response at the fundament mode was still dominant later in flight, although the overall level was lower. During flight, the spectrum constantly changed; however, there were particular tonal components, such as the acoustic modes, that appeared to be consistently high in amplitude. This emphasizes the importance of attenuating the fundamental mode.

The acceleration measured by the onboard axial telemetry accelerometer is presented in Fig. 17 for the first 90 s of flight. The second-stage ignition is easily recognizable at 20 s. The acceleration changed constantly during assent, which resulted in the constantly changing acoustic spectrum. Figure 18 presents the power spectral density of the acceleration signal computed using data over the first second. The plot displays large amplitude acceleration in the vicinity of the acoustic peak shown in Fig. 15 at 127 Hz. Although no distinct

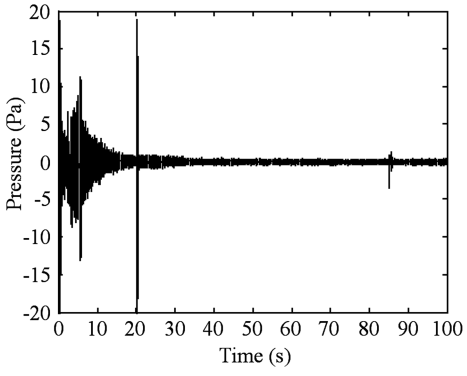

Fig. 13 Time history measured from a microphone in VALPE-1.

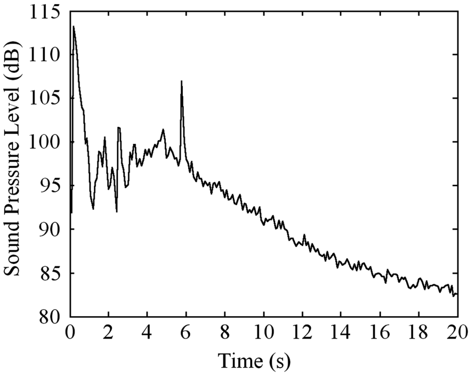

Fig. 14 Spatially averaged interior sound pressure level from VALPE-1.

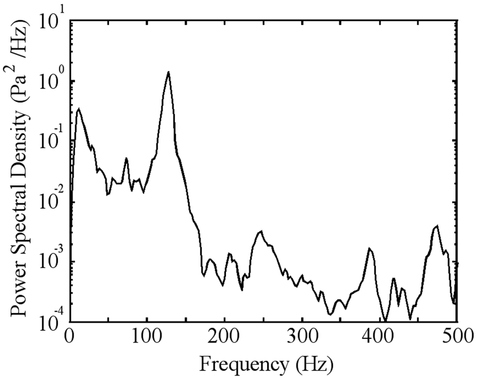

Fig. 15 Power spectral density of the spatially averaged response from VALPE-1 for the first second after launch.

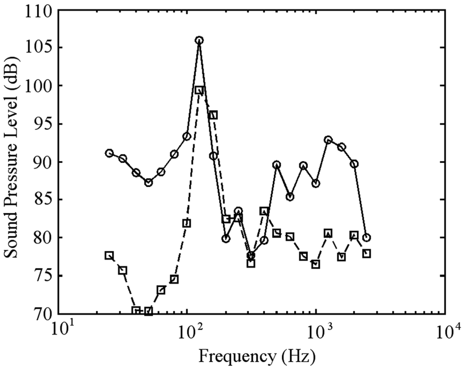

Fig. 16 Averaged response over one-third-octave bandwidths: -○-, 0–1 s; -□-, 20–21 s.

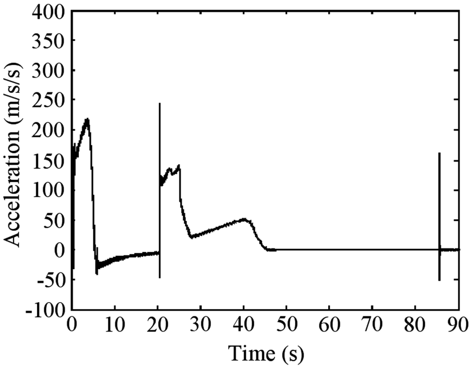

Fig. 17 Measured acceleration from VALPE-1.

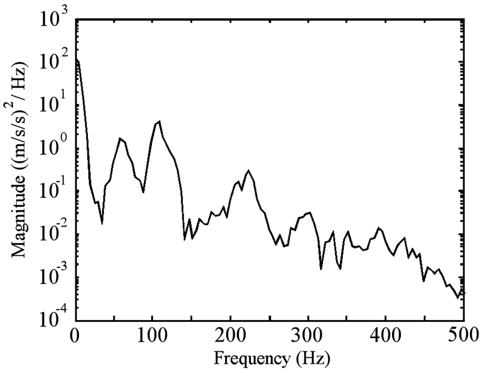

Fig. 18 Power spectral density of acceleration data from VALPE-1 for the first second after launch.

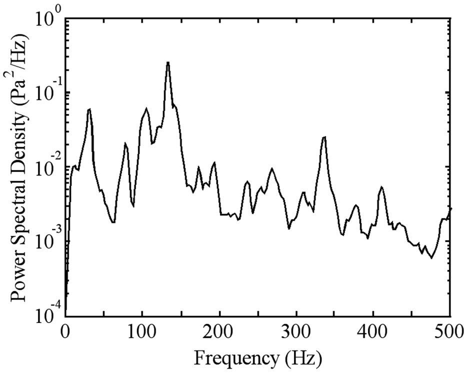

Fig. 21 Power spectral density of the spatially averaged response from VALPE-2 for the first second after launch.

peak is shown at 138 Hz, the resonance observed during test, there is significant amplitude in this frequency region.

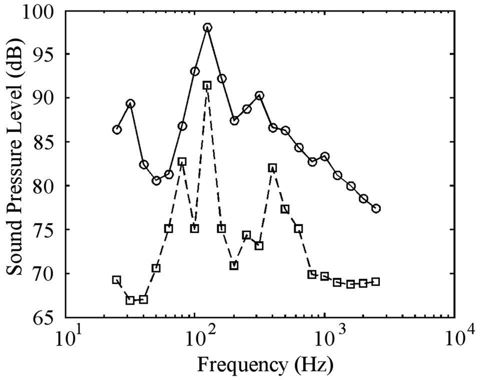

Fig. 22 Averaged response over one-third-octave bandwidths: -○-, 0–1 s; -□-, 20–21 s.

B. VALPE-2 Results

The sensor suite for VALPE-2 was similar to that used in VALPE-1. The time history for a single microphone located in the forward part of the fairing is given in Fig. 19. The second-stage ignition is apparent at $T = 20$ s. The spatially averaged interior sound pressure level (computed over 0.1 s intervals) as a function of time for the first 20 s is presented in Fig. 20. The maximum response indicated in Fig. 20 was 102.4 dB, which occurred at launch. The spectrum of the spatially averaged response during the first second after launch is given in Fig. 21. The first acoustic mode occurred at 133 Hz; it appears that the second acoustic resonance occurred at 269 Hz and the third at 336 Hz. Changes in acoustic resonance frequencies (relative to VALPE-1) likely resulted primarily from the presence of the various experiments and to a lesser extent from changes in temperature and humidity between launches. These provided different volumetric fill factors and may have coupled with the acoustic resonances. As in VALPE-1, there were several other peaks in the spectrum, likely attributable to the acceleration spectrum. The wide amplitude difference observed in the PSD between the fundamental and higher order modes noted for VALPE-1 was not observed in VALPE-2.

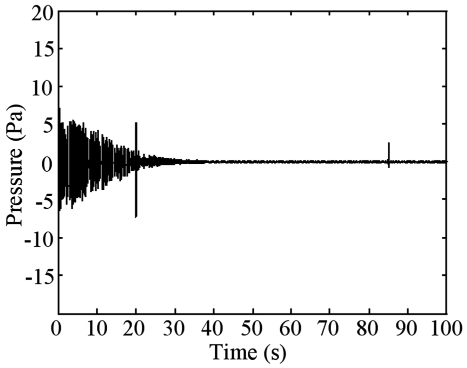

Fig. 19 Time history measured from a microphone in VALPE-2.

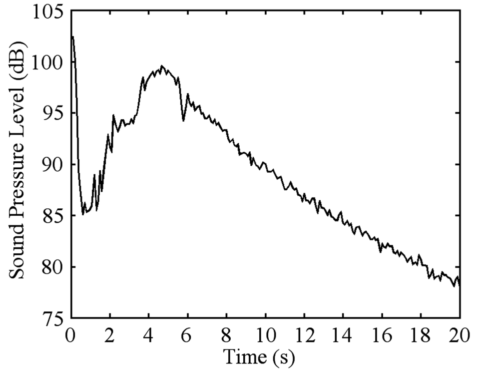

Fig. 20 Spatially averaged interior sound pressure level from VALPE-2.

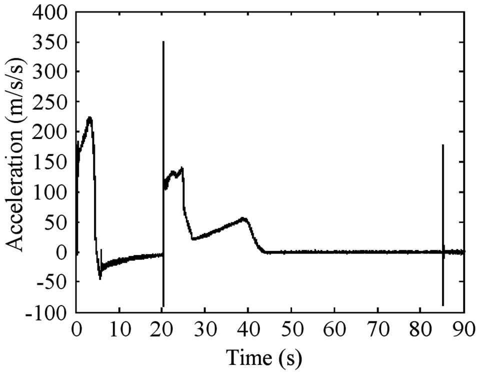

Fig. 23 Measured acceleration from VALPE-2.

Figure 22 presents the spatially averaged sound pressure level (computed over one-third-octave bands) for the first second of launch and for the interval from 20 to 21 s. The overall sound pressure level was 102.2 dB from 0 to 1 s and 93.2 dB from 20 to 21 s. In contrast to VALPE-1 (Fig. 16), there was less response above 500 Hz, likely due to the presence of the other experiments within VALPE-2 that may have provided additional acoustic damping.

The time history from the axial telemetry accelerometer is given in Fig. 23. The second-stage ignition is apparent at 20 s, as is the second-stage separation at about 85 s. The power spectral density plot for this signal is given in Fig. 24 (computed over the 20–40 s

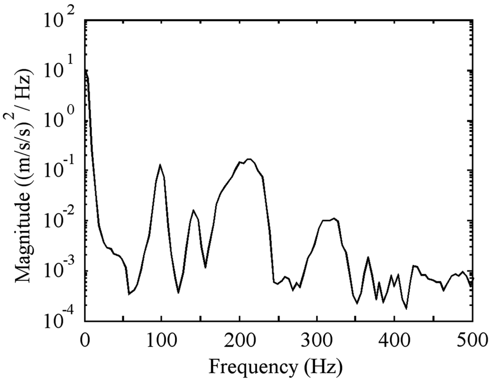

Fig. 24 Power spectral density of acceleration data from VALPE-2: 20–40 s.

interval). The dominant peak occurred at 69 Hz, the second at 136.6 Hz (proximal to the fundamental acoustic resonance), and the third at 219 Hz.

Immediately before launch, the acoustic control system was tested by playing a filtered white noise acoustic disturbance through a large subwoofer on the exterior of the fairing. The white noise was filtered by a 138 Hz, second-order bandpass filter with 10% damping to approximately represent the shaping of the sound input by the nose-cone resonance. The results of this test, as measured by the payload microphone, are shown in Fig. 25.

The reduction in acoustic pressure achieved over the 50–400 Hz bandwidth by inserting the device was 4.5 dB rms. Closing the loop on the active control system resulted in an additional 2.3 dB rms reduction over the same range, yielding a 6.8 dB rms total reduction due to the introduction of the active device.

In Fig. 26, the PSDs of the measured response from the forward-center microphone of VALPE-1 are compared with the measured response from the "control" microphone of VALPE-2. Unfortunately, there was an intermittent failure of the power system for the active control experiment on VALPE-2, causing it to be inactive for the first 20 s of flight. The system did recover around 20 s into the flight. The data shown represents the 21–40 s interval of flight, during which most clipping and dropout events had subsided. These sensor signals make a good comparison because they were in approximately the same location during each flight. A comparison of the two measurements indicates an 8.8 dB rms reduction in the acoustic level from 20 to 300 Hz.

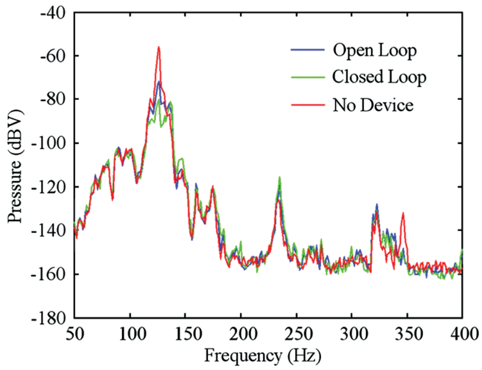

Fig. 25 Ground test of device immediately before launch.

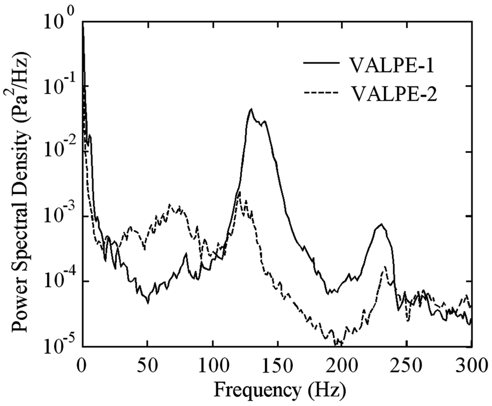

Fig. 26 Comparison of power spectral density plots of microphone measurements from VALPE-1 and VALPE-2.

VI. Conclusions

This paper presented the development and application of an active acoustic absorber to attenuate low-frequency acoustic resonances in a payload fairing. The device was integrated into the second of two sounding rocket experiments, and performance was inferred by comparing test data from each flight. It was hypothesized that acceleration of the nose-cone bulkhead was a significant source of the internal fairing noise. Accordingly, a model was developed of the structural-acoustic system incorporating the effect of the fundamental mode of the nose-cone and fairing assembly. This model explained the relative dominance of the first acoustic mode in comparison with the response of the rest of the bandwidth observed in VALPE-1.

The electromechanical dynamics of the acoustic absorber were coupled with the payload structural-acoustic model and used to simulate the active control system. In simulations, some reduction of the fundamental acoustic resonance was realized using the device passively (i.e., from simply coupling the device with the acoustic volume). More noise reduction was achieved by adding a low-order active damping feedback controller based on the positive-position feedback control approach used in structural vibration control applications.

Simulations on the coupled fairing and actuator system model demonstrated the feasibility of using multiple control laws for targeting more than the first two acoustic resonances. Secondary control laws were designed and implemented using a sequential loop closure, which was also used on the flight experiment. Tuning rules and optimization schemes were presented that could be autonomously implemented on the sounding rocket.

A prototype device was constructed and tested in laboratory experiments. Upon boot up of the stand-alone control computer, algorithms were executed to autonomously identify the appropriate design frequencies, damping ratios, and feedback gains of the controller. Flight qualification tests were very demanding, and many components (experiment hardware, sensors, signal conditioners, power sources) suffered damage and had to be replaced before launch.

The measured data from both VALPE-1 and VALPE-2 indicated a constantly changing environment, both in spectral content and amplitude. Nevertheless, a frequency analysis of data indicated the relative contributions of the acoustic resonance frequencies. The cause of the relatively high amplitude of the fundamental acoustic mode in VALPE-1 was the proximity of the fundamental nose-cone "bounce mode" to the fundamental acoustic mode. Although the acceleration profile of the launch vehicle was constantly changing throughout flight, yielding a constantly changing acoustic spectrum, the tonal content at acoustic resonance frequencies was persistent.

VALPE-2 showed the first successful demonstration of an active noise control system on a payload fairing. Launches were under nearly identical environmental conditions, using similar rocket motors and similar sensor packages. Data from VALPE-2 clearly showed an overall reduction in the interior acoustic levels as measured by the spatially averaged interior microphone response. A comparison of the response measured at nearly identical microphone locations (no spatial averaging) on VALPE-1 and VALPE-2 indicated an 8.8 dB overall reduction in the acoustic levels computed from 20 to 300 Hz for a 19 s time interval. A nearly 1 order of magnitude reduction was measured at the first acoustic resonance frequency. The acoustic attenuation was directly attributable to the presence of the active acoustic absorber. These flight experiments demonstrate the feasibility of an active acoustic control approach for low-frequency acoustic attenuation in payload fairings.

References

[1] Agrawal, B. N., *Design of Geosynchronous Spacecraft*, Prentice–Hall, Englewood Cliffs, NJ, 1986, pp. 184–189.

[2] Sarafin, T. P. (ed.), *Spacecraft Structures and Mechanisms from Concept to Launch*, Microcosm, Inc., El Segundo, CA, 1995, pp. 16–19, 42–51, 508–511.

[3] Delta-IV Payload Planners Guide, MDC 99H0065, The Boeing Company, Huntington Beach, CA, 1999.

[4] Taurus Launch System Payload User's Guide, Release 3.00, Orbital Sciences Corporation, Dulles, VA, 1999.

[5] Ariane 5 User's Manual, Issue 4, Revision 0, Arianespace, Evry-Courcourones Cedex, France, 2004.

[6] Tanner, C. S., "Lessons Learned in Predicting Launch Vehicle Vibroacoustic Environments," *Journal of the Institute of Environmental Sciences*, Vol. 40, No. 2, 1997, pp. 38–42.

[7] Thomas, V. C., "Vibroacoustic Database Management Center for Shuttle and Expendable Launch Vehicle Payloads," *Journal of Environmental Sciences (China)*, Vol. 30, No. 6, 1987, pp. 24–26.

[8] Griffin, S., Lane, S. A., Clark, R. L., and Kemp, J. D., "Innovative Passive Mechanism for Control of Low-Frequency Transmitted Sound into a Launch Vehicle Fairing," , AIAA Paper 2000-1436, April 2000.

[9] Griffin, S., and Lane, S. A., "Passive Vibroacoustic Attenuator for Structural Acoustic Control," U. S. Patent #6,195,442, filed Aug. 27, 1999, issued February 27, 2001.

[10] Lane, S., Richard, R., Griffin, S., "Fairing Noise Control Using Passive Vibroacoustic Attenuation Devices," *Journal of Spacecraft and Rockets*, Vol. 43, No. 1, 2006, pp. 31–44.

[11] Esteve, S., and Johnson, M., "Reduction of Sound Transmission into a Circular Cylindrical Shell Using Distributed Vibration Absorbers and Helmholtz Resonators," *Journal of the Acoustical Society of America*, Vol. 112, No. 6, 2002, pp. 2840–2848.
doi:10.1121/1.1514933

[12] Fahy, F. J., and Schofield, C., "A Note on the Interaction Between a Helmholtz Resonator and an Acoustic Mode of an Enclosure," *Journal of Sound and Vibration*, Vol. 72, No. 3, 1980, pp. 365–378.
doi:10.1016/0022-460X(80)90383-1

[13] Cummings, A., "The Effect of a Resonator Array on the Sound Field in a Cavity," *Journal of Sound and Vibration*, Vol. 154, No. 1, 1992, pp. 25–44.
doi:10.1016/0022-460X(92)90402-J

[14] Lane, S., and Clark, R., "Dissipative Feedback Control of a Reverberant Enclosure Using a Constant Volume Velocity Source," *Journal of Vibration and Acoustics*, Vol. 120, No. 4, 1998, pp. 987–993.
doi:10.1115/1.2893931

[15] Olson, H. F., and May, E. G., "Electronic Sound Absorber," *Journal of the Acoustical Society of America*, Vol. 25, No. 6, 1953, pp. 1130–1136.
doi:10.1121/1.1907249

[16] Radcliffe, C. J., Gogate, S. D., and Hall, G., "Development of an Active Acoustic Sink for Noise Control Applications," *ASME Active Control of Vibration and Noise*, Vol. 75, 1994, pp. 43–50.

[17] Denoyer, K. K., Griffin, S. F., and Sciulli, D., "Hybrid Structural/Acoustic Control of a Sub-Scale Payload Fairing," *Proceedings of the SPIE, Smart Structures and Integrated Systems*, Vol. 3329, edited by M. E. Regelbrugge, International Society for Optical Engineering, Bellingham, WA, July 1998, pp. 237–243.

[18] Lane, S. A., Clark, R. L., and Southward, S. C., "Active Control of Low Frequency Modes in an Aircraft Fuselage Using Spatially Weighted Arrays," *Journal of Vibration and Acoustics*, Vol. 122, No. 3, 2000, pp. 227–234.
doi:10.1115/1.1303848

[19] Lane, S. A., Kemp, J. D., Griffin, S., and Clark, R. L., "Active Acoustic Control of a Rocket Fairing Using Spatially Weighted Transducer Arrays," *Journal of Spacecraft and Rockets*, Vol. 38, No. 1, 2001, pp. 112–119.
doi:10.2514/2.3662

[20] Griffin, S., Lazzaro, A., Henderson, K., and Lane, S., "Development of an Adaptive Passive Vibro-Acoustic Device for Payload Fairings," AIAA Paper 2003-1814, April 2003.

[21] Henderson, K., Lane, S., Gerhart, C., and Richard, R., "Overview of the Vibro-Acoustic Launch Protection Experiment at Air Force Research Laboratory," *SPIE Smart Structures and Materials Conference*, International Society for Optical Engineering, Bellingham, WA, March 2003, pp. 66–72.

[22] Gardonio, P., Ferguson, N., and Fahy, F., "Modal Expansion Analysis of Noise Transmission Through Circular Cylindrical Shell Structure with Blocking Masses," *Journal of Sound and Vibration*, Vol. 244, No. 2, July 2001, pp. 259–297.
doi:10.1006/jsvi.2000.3456

[23] Griffin, S., Lane, S. A., Hansen, C., and Cazzolato, B., "Active Structural Acoustic Control of a Rocket Fairing Using Proof-Mass Actuators," *Journal of Spacecraft and Rockets*, Vol. 38, No. 2, 2001, pp. 219–225.
doi:10.2514/2.3673

[24] Fanson, J. L., and Caughey, T. K., "Positive Position Feedback Control for Large Space Structures," *AIAA Journal*, Vol. 28, No. 4, 1990, pp. 717–724.
doi:10.2514/3.10451

[25] Friswell, M. I., and Inman, D. J., "The Relationship Between Positive Position Feedback and Output Feedback Controllers," *Smart Materials and Structures*, Vol. 8, No. 3, June 1999, pp. 285–291.
doi:10.1088/0964-1726/8/3/301

[26] Bronowicki, A. J., Abhyankar, N. S., and Griffin, S. F., "Active Vibration Control of Large Optical Space Structures," *Smart Materials and Structures*, Vol. 8, No. 6, Dec. 1999, pp. 740–752.
doi:10.1088/0964-1726/8/6/304

[27] MATLAB® Ver. 7.0.4, The Math Works, Inc., Natick MA, 2005.

[28] Simulink Version 6.2, The Math Works, Inc., Natick MA, 2005.

L. Peterson
Associate Editor